JOURNAL OF GEOPHYSICAL RESEARCH, VOL. 114, F03006, doi:10.1029/2008JF001127, 2009

Setting the length and time scales of a cellular automaton dune model from the analysis of superimposed bed forms

C. Narteau,[1] D. Zhang,[1] O. Rozier,[2] and P. Claudin[3]

Received 1 August 2008; revised 30 April 2009; accepted 29 May 2009; published 28 July 2009.

[1] We present a new 3-D cellular automaton model for bed form dynamics in which individual physical processes such as erosion, deposition, and transport are implemented by nearest neighbor interactions and a time-dependent stochastic process. Simultaneously, a lattice gas cellular automaton model is used to compute the flow and quantify the bed shear stress on the topography. Local erosion rates are assumed to be proportional to the shear stress in such a way that there is a complete feedback mechanism between flow and bed form dynamics. In the numerical simulations of dune fields, we observe the formation and the evolution of superimposed bed forms on barchan and transverse dunes. Using the same model under different initial conditions, we perform the linear stability analysis of a flat sand bed disturbed by a small sinusoidal perturbation. Comparing the most unstable wavelength in the model with the characteristic size of secondary bed forms in nature, we determine the length and time scales of our cellular automaton model. Thus, we establish a link between discrete and continuous approaches and open new perspectives for modeling and quantification of complex patterns in dune fields.

Citation: Narteau, C., D. Zhang, O. Rozier, and P. Claudin (2009), Setting the length and time scales of a cellular automaton dune model from the analysis of superimposed bed forms, *J. Geophys. Res.*, *114*, F03006, doi:10.1029/2008JF001127.

1. Introduction

[2] Sand dunes form magnificent large patterns whose symmetries reflect those of the wind regime and whose appearance also depends on the amount of sand available for transport as well as the possible presence of vegetation [*McKee*, 1979; *Breed and Grow*, 1979; *Lancaster*, 1995; *Bristow et al.*, 2000; *Wiggs*, 2001; *Kocurek and Ewing*, 2005; *Ewing et al.*, 2006; *Baas and Nield*, 2007]. These dune patterns present various length scales, from an ''elementary'' size, on the order of 20 m, perceivable as the typical dimension of the smallest superimposed structures [*Elbelrhiti et al.*, 2005], to the largest features, which can reach a kilometric scale (Figure 1). Because smaller structures propagate faster, dunes interact with each other, leading to the emergence of complex patterns by amalgamation or nucleation of secondary bed forms [*Kocurek et al.*, 1991; *Elbelrhiti et al.*, 2005, 2008].

[3] Continuous dune models have recently been developed and are able to generate realistic dune shapes under various conditions [*Kroy et al.*, 2002a, 2002b; *Andreotti et al.*, 2002; *Hersen*, 2004; *Durán and Herrmann*, 2006; *Parteli and Herrmann*, 2007]. They encode basic physical mechanisms responsible for the formation and propagation of dunes and, in addition to morphological features, they are also able to predict how the characteristic wavelength for the formation of dunes scales with physical properties of granular materials and fluids [*Claudin and Andreotti*, 2006]. However, the precise way in which dunes interact, amalgamate or calve is not well reproduced by these models [*Hersen et al.*, 2004; *Durán et al.*, 2005]. In particular, the modeling of secondary bed forms induced by collisions, which are probably important for size regulation in barchan fields, is presently an open issue [*Elbelrhiti et al.*, 2005, 2008]. A definite weakness in these models is the way the recirculation bubbles on the lee side of dunes are taken into account by means of an effective envelope; the complete determination of the flow over a complex topography is numerically too expensive. As a result, they cannot be run accurately over long time periods to investigate the dynamics of a significant portion of a dune field.

[4] Cellular automaton (CA) dune models are more appropriate for this purpose [*Nishimori and Ouchi*, 1993; *Werner*, 1995; *Werner and Kocurek*, 1997; *Nishimori et al.*, 1999; *Momiji and Warren*, 2000]. These discrete models consist of 2-D regular rectangular lattices in which the local height of sediment is measured as the accumulation of so-called ''sand slabs.'' The surface topography evolves through individual motion of these slabs according to a set of transition rules. Thus, CA dune models can be run in a very efficient way, and a large diversity of bed forms can arise spontaneously from collective behaviors of interacting

[1] Laboratoire de Dynamique des Fluides Géologiques, UMR 7154, Institut de Physique du Globe de Paris, Université Paris 7, CNRS, Paris, France.

[2] Service Informatique, UMR 7154, Université Paris 7, Institut de Physique du Globe de Paris, CNRS, Paris, France.

[3] Laboratoire de Physique et de Mécanique des Milieux Hétérogènes, UMR 7636, Université Paris 7, École Supérieure de Physique et de Chimie Industrielles de la Ville de Paris, CNRS, Paris, France.

0148-0227/09/2008JF001127$09.00

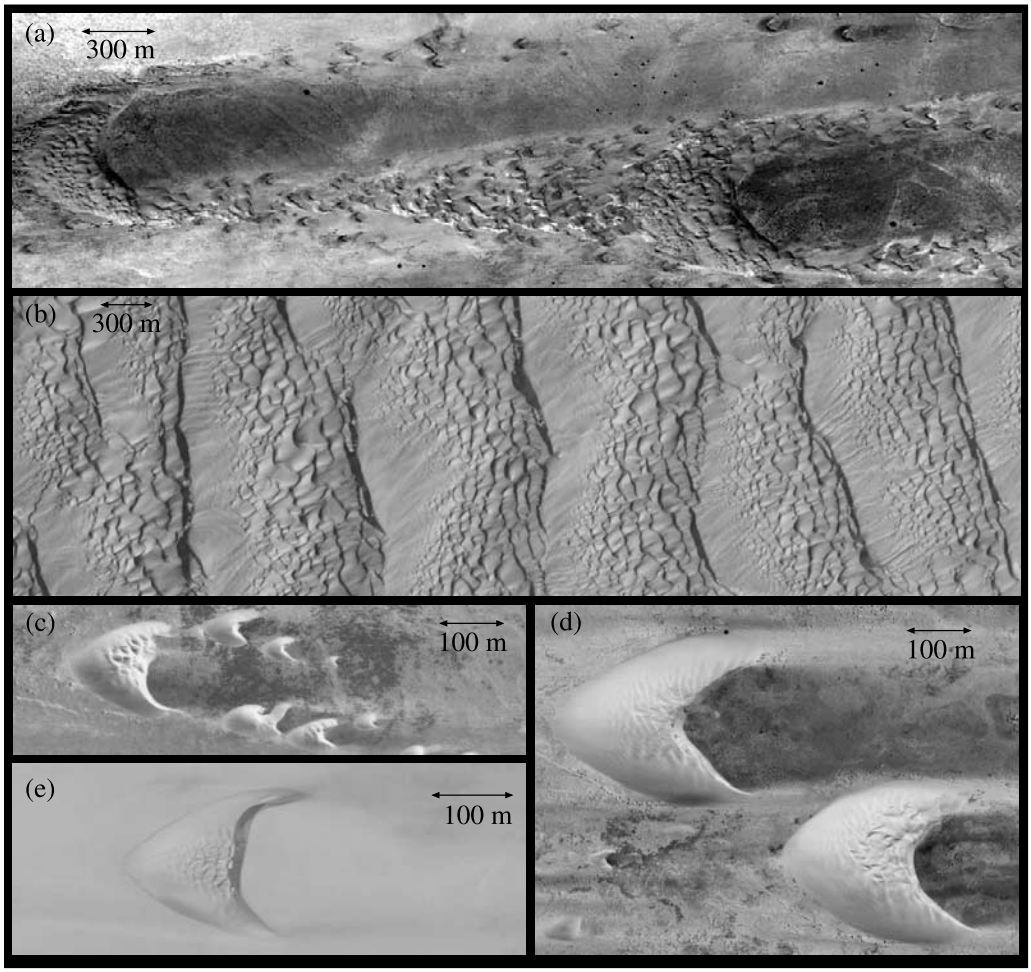

Figure 1. Observations of superimposed dune patterns in nature for (a) megabarchans in Peru (6°08′47.39″S 80°50′25.47″W), (b) transverse dunes in Namibia (26°6′26.21″S 15°00′23.90″W), (c) barchan dunes in Morocco (27°32′49.52″N 13°12′40.15″W), (d) barchan dunes in Morocco (21°36′51.45″N 16°46′09.86″W), and (e) isolated barchan in Peru (9°5′0.58″S 78°30′39.85″W).

cells over time. However, as for all CA approaches [*Wolfram*, 1986; *Chopard and Droz*, 1998], these discrete numerical simulations present two types of drawbacks. First, transition rules do not correspond to real physical mechanisms which would have an existence at microscopic length scales. Therefore, these rules are pure phenomenological parameters whose relevance is only controlled a posteriori by the effects they induce on the model outputs. The second flaw is due to the discrete structure of CA: nothing imposes what the size of a sand slab must be. As a result, time and length scales are arbitrary inputs of CA dune models. This problem is particularly evident when, beyond the overall symmetry of the dune pattern, one wishes to address scale related issues such as coarsening (i.e., dune amalgamation).

[5] In this paper we present a new class of cellular automaton model for sand dunes, which couples a modeling of sand slabs in the spirit of traditional CA models and a lattice gas description of the turbulent air flow [*Frisch et al.*, 1986; *d'Humières et al.*, 1986]. Our model is powerful enough to generate realistic large barchan or transverse dunes with superimposed bed forms. As in nature, these superimposed structures appear at regular and well-defined intervals, and we can make use of this secondary bed forms to set the length scale of our model. With such a length scale, sand fluxes and shear velocity can be used to determine the time scale of this cellular automaton approach. This model at hand, we are then ready to investigate in a quantitative way the dynamics of dune fields, an issue which is however beyond the scope of this paper.

[6] The rest of the paper is structured as follows. In order to state the physical concepts on which the analysis of this work is based, we start with a brief pedagogical review of dune formation as a result of a linear instability. In section 3, we describe the CA model and emphasize the differences and improvements with respect to the previous works. Nevertheless, most of the technical details of the numerical procedures are gathered in the appendices. Then, we present some distinctive dune patterns produced by the model (section 4). In connection to the continuous approaches, section 2 is devoted to the stability analysis of a flat sand bed in order to determine the most unstable wavelength in the model. Finally, we discuss the perspectives of this work,

namely, as mentioned above, the emergence and the evolution of complex patterns in dune fields.

2. Dunes as the Result of a Linear Instability: A Brief Review

[7] As one of the main goal of this paper, the setting of the length and time scales of a CA dune model, is deeply linked to the analysis of dune formation as a linear instability, we devote a brief pedagogical section to the relevant physical mechanisms involved in this problem. Such a section is important because the community working on aeolian dunes is composed of scientists with various backgrounds, so that concepts and terminology can be rather varied. In what follows, the term ''instability'' characterizes the emergence and growth of a pattern in an initially homogeneous system. Conversely, ''stability'' refers to the ability of a system to stay in its homogeneous state, or to return to it when perturbed.

2.1. Linear Stability Analysis

[8] The analysis of the time and length scales of instabilities by means of linearized equations is a standard approach in hydrodynamics and many other branches of physics. By identifying stabilizing and destabilizing terms, these analyses reveal the mechanisms that, starting from a homogeneous system, spontaneously generate periodic patterns. Examples of such instabilities are countless; the formation of an undulation along a flat interface between two fluids is a case in point.

[9] In a vast majority of cases, the primary pattern emerges with a well defined wavelength λ. At the early stage of this instability (the linear regime) λ stays constant with time t, whereas the amplitude ζ of the pattern (the amplitude of the interface undulations in the above example) grows exponentially $\zeta(t) \propto \exp(\sigma t)$. In this expression, σ is the growth rate with units of frequency. In order to analyze such an instability and to understand why a particular wavelength is emerging, it is necessary to estimate the so-called dispersion relation $\sigma(k)$, which gives the growth rate value of a sinusoidal perturbation as a function of the wave number $k = 2\pi/\lambda$. A positive σ value corresponds to a perturbation that grows (unstable situation), whereas decaying (stable) perturbations have $\sigma < 0$. As an initial flat interface actually contains, in the form of an infinitesimal ''noise,'' all possible wave numbers, the dominant wavelength of an emerging pattern corresponds to the most unstable mode, i.e., to the largest positive σ value. We call this selected length scale λ_{max}. The corresponding time scale is then $1/\sigma_{max}$. Beyond this initial stage, the pattern usually exhibits coarsening of the wavelength and saturation of the amplitude that are not accounted for by this linear analysis. Indeed, numerical models have to come into play to explore complex dune interactions.

[10] In nature and in laboratory experiments, it is usually possible to measure the values of λ_{max} and σ_{max} under various conditions. As the linear analysis of the governing equations permit the expression of these quantities as functions of the different parameters of the system, a direct test of understanding of the instability is to investigate whether or not they scale as predicted with these parameters.

2.2. Dune Instability Mechanism

[11] In the context of sediment transport, linear stability analyses were performed several decades ago for the formation of ripples and dunes on the bed of sandy rivers [*Kennedy*, 1963; *Reynolds*, 1965; *Engelund*, 1970; *Fredsøe*, 1974; *Richards*, 1980; *Engelund and Fredsøe*, 1982]. These works have demonstrated that a key ingredient to understand how a flat sand bed can destabilize is the shift between the flux of sediment $q(x)$ and the topography $z(x)$, where x is the along-stream coordinate. Around a positive and smooth topographic feature such as a bump or a dune, the location of the maximum of q separates an upstream erosion zone from a downstream deposition zone. Then, a perturbation of the bed can grow if the crest is in the deposition zone. Therefore, all mechanisms that make the flux phase advanced have a destabilizing action, whereas those by which q responds with a lag are stabilizing.

[12] Determination of the maximum flux of sediment can be decomposed into two independent components. As the driving force that makes the sediment of the bed move is the basal shear stress, a first contribution is of pure aerodynamical nature: what is the shear stress imposed by the flow on the bed? The second one is a transport issue: how does the flux adjust to an imposed shear stress?

[13] In order to study wind profiles over low hills, *Jackson and Hunt* [1975] and followers have developed a linear description of turbulent flows over flat obstacles [*Sykes*, 1980; *Taylor et al.*, 1987; *Hunt et al.*, 1988]. A robust feature is that the flow can be divided into the following three layers: (1) an outer layer, where the fluid can be considered as inviscid (the inertial terms balance the pressure gradient); (2) an inner layer, where the inertial terms are negligible, (stress and pressure gradients balance); and (3) a surface layer, which is responsible for the aerodynamical roughness. Because of turbulent dissipation and fluid inertia, an upwind shift between the shear stress and the topography is generated at the matching region between the outer and the inner layers, so that the basal shear stress is in advance with respect to the bed.

[14] Many studies have been devoted to the relation between shear stress and sediment transport, providing numerous models as well as empirical data fits [*Meyer-Peter and Müller*, 1948; *Bagnold*, 1956; *Ungar and Haff*, 1987; *Anderson and Haff*, 1988; *Rasmussen et al.*, 1996; *Sauermann et al.*, 2001; *Andreotti*, 2004]. Regarding sediment transport, it is extremely important to distinguish between steady/homogeneous and transient situations. In steady state, one can evaluate the influence of the shear stress magnitude τ_s on the value of the sediment flux. One can also investigate the role of bed slope and cohesion on the threshold shear stress value for motion inception τ_c. In all cases, the sediment flux converges toward an equilibrium value which is described as being ''saturated.'' Then, transport laws precisely specify the expression of the function $Q_{sat}(\tau_s, \tau_c)$.

[15] In nonhomogeneous or unsteady situations, however, the actual flux q does not immediately adjust to the local value of the shear stress. It needs some space or time to reach its equilibrium value Q_{sat}. This phenomenon can be described as a relaxation process toward saturation of the sediment flux. It was early observed and measured by *Bagnold* [1941], and modeled by *Sauermann et al.* [2001]

using a nonlinear equation. Such a relaxation mechanism is not specific to the physics of sediment transport, but a rather generic behavior of out of equilibrium systems. Usually a single characteristic length (here the saturation length l_{sat}) or time is used to describe it as a first-order process. Importantly, this relaxation cannot be correctly described purely by a shift between q and τ_s, as initially proposed by *Kennedy* [1963] in the context of river dune formation. Correcting this conceptual mistake, a linear first-order saturation equation (an exponential relaxation toward equilibrium) was introduced by *Parker* [1975]. Such a linear description of the saturation was also adopted by *Andreotti et al.* [2002]. In summary, the sediment flux is always delayed with respect to the basal shear stress.

2.3. Saturation Length and Dune Size

[16] Combining these different ingredients in a set of differential equations, the linear stability analysis shows that the wavelength for the nucleation of dunes scales essentially with the saturation length $\lambda_{max} \propto l_{sat}$ [*Andreotti et al.*, 2002]. As turbulence is almost scale invariant, the aerodynamical roughness marginally affects the value of the most unstable mode (A. Fourrière et al., Ripples and dunes in a turbulent stream; Part 1, Turbulent flow over topography; Part 2, Evidences against the formation of river dunes by primary linear instability, submitted to *Journal of Fluid Mechanics*, 2009, hereinafter referred to as Fourrière et al., submitted manuscript, 2009a and 2009b, respectively). Similarly, the effect of bed slope significantly modifies λ_{max} only very close to the transport threshold (Fourrière et al., submitted manuscript, 2009b; B. Andreotti et al., Measurements of the aeolian sand transport saturation length, submitted to *Geomorphology*, 2009).

[17] Discussion of the physical mechanisms responsible for the saturation, i.e., the determination of the parameters that control l_{sat}, is a separate issue. Grain inertia may be a relevant hypothesis as it explains the main difference of dune size in aeolian, subaqueous and Martian conditions [*Claudin and Andreotti*, 2006]. In this case, $l_{sat} \propto (\rho_s/\rho_f)d$, where ρ_s/ρ_f is the grain to fluid density ratio and d is the grain diameter. Nevertheless, other mechanisms have been proposed for subaqueous ripples by *Charru* [2006] and for Martian dunes by *Parteli and Herrmann* [2007] (see also *Andreotti and Claudin* [2007] and *Parteli et al.* [2007a]).

[18] This important debate is however unrelated to the purpose of the present paper. Instead, as λ_{max} and σ_{max} are the natural length and time scales of the instability, the idea is to estimate the dispersion relation of our CA dune model. Then, the most unstable wavelength in the numerical simulations may be directly compared to in situ measurements of this quantity.

[19] How can one get a good estimate of λ_{max} from field data? Once again, λ_{max} is not the size of a single (developed) dune, but, strictly speaking, the wavelength of a dune pattern emerging from a flat bed. Emerging dunes are in fact generically present as superimposed patterns on the flanks of large enough dunes, such as barchans [*Elbelrhiti et al.*, 2005]. λ_{max} can then be computed as an ensemble average of the crest to crest distances of these superimposed undulations. A typical value measured on the barchans of Atlantic Sahara is $\lambda_{max} \simeq 20$ m.

[20] That does not mean that smaller dunes cannot be observed. As a result of a complex interaction between larger dunes, some small, disappearing structures may be observed locally. In addition, and more importantly for our present purpose, λ_{max} is the wavelength of the most but not the only unstable mode. In fact, the unstable range includes all large wavelengths down to a cutoff λ_c, which corresponds to a vanishing growth rate, $\sigma(k_c) = 0$. Interestingly, λ_c also scales with l_{sat} as it is roughly a fraction (a half) of λ_{max} [*Andreotti et al.*, 2002]. This cutoff value can be interpreted as the typical size of the smallest dunes [*Kroy et al.*, 2002a, 2002b]. This is consistent with Bagnold's observation that very small dunes are on the order of 10 m long [*Bagnold*, 1941]. On the other hand, after the superimposed pattern has emerged, it quickly leaves the linear regime and starts coarsening. This is why the measure of the average distance between secondary slip faces superimposed on very large dunes can give larger values than the above 20 m. For example, we measured around 35 m on megabarchans of Atlantic Sahara [*Elbelrhiti et al.*, 2005]. In summary, although the determination of the value of λ_{max} from field data is inevitably subjected to some uncertainty, an average and typical value between 10 and 35 m seems to be reasonable.

3. Model

[21] A cellular automaton for sediment transport is coupled with a lattice gas cellular automaton model (LGCA) in order to mimic the interplay between the bed form dynamics, the fluid flow and the bed shear stress. Despite the additional challenge we face in coupling both models together, a major advantage of such a hybrid modeling is to eliminate some arbitrary descriptions of the flow. Then, local dependencies on flow patterns and the impact of sediment motions on the transport capacity can be explicitly taken into account.

3.1. A 3-D Cellular Automaton Model for Sediment Transport

[22] A 3-D regular rectangular lattice is used to compute the evolution of a layer of erodible sediment lying on a flat bedrock. The aspect ratio of an elementary cell is a parameter of the model (see section A1). Here, for numerical efficiency in the coupling between this sediment transport model and the LGCA, an elementary cell is a cube of edge length l_0 and not a slab of sediment as is usually the case in cellular automaton models for dune dynamics [*Nishimori and Ouchi*, 1993; *Werner*, 1995].

[23] The indices (i, j, k), $i \in [1, L]$, $j \in [1, L]$, $k \in [1, H]$ are the labels of the Cartesian coordinates. The cell $c_{i,j,k}$ can be in one of the following three states: (1) a volume of fluid, (2) an immobile volume of sediment, and (3) a volume of sediment in motion. For the sake of simplicity, the two sedimentary states have the same density, and they differ only in their ability to move.

[24] The entire dynamics are controlled by the three states through local interactions between neighboring cells. We consider only nearest neighbor interactions and an elementary cell may change state only if it shares a boundary with a neighboring cell in a different state. These pairs of nearest neighbor cells are called "doublet." Thus, we analyze an

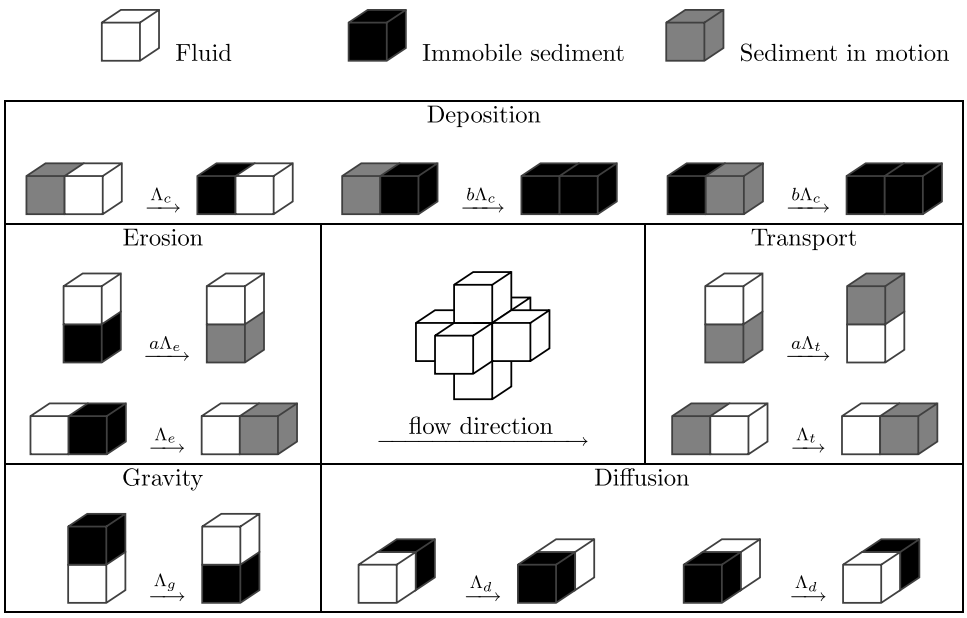

Figure 2. Active transitions of doublets in the cellular automaton model for sediment transport. Different sets of transition are associated with deposition, erosion, transport, gravity, and diffusion. Here $\{\Lambda_c, \Lambda_e, \Lambda_t, \Lambda_g, \Lambda_d\}$ are transition rates with units of frequency; a and b are positive constants. The central inset shows the direction of the flow and the orientation of the nearest neighbors in a regular cubic lattice.

evolving population of doublets over time. Nevertheless, all the possible configurations of doublet do not lead to a change in state, and with respect to the physics of sediment transport, we use only a limited number of transitions from one configuration to another. Overall, in order to ensure mass conservation, these transitions do not modify the number of sedimentary cells.

[25] We isolate individual physical processes and associate each of them with a specific set of transitions according to the direction of the flow. Thus, erosion and deposition phases are not joined into a more general "saltation rule" as is the case in classical cellular automaton models for dune dynamics. Instead, as shown in Figure 2, we have transitions for

[26] 1. Erosion, which is the initiation of movement of a sediment layer due to the bed shear stress imposed by the flow. This erosion process does not discriminate between different grain motions (i.e., saltation and reptation). Nevertheless, it involves transitions in horizontal and vertical directions to account for drag and lift forces that initiate grain movement.

[27] 2. Transport, which is the motion of sediment. Mobile sediment layers can be transported upward and in the direction of the flow.

[28] 3. Deposition, which is the end of sediment movement. This deposition process is enhanced by topographic obstacles and occurs faster on slopes of preexisting structures.

[29] 4. Gravity, which is the fall of sediment under its own weight. Gravity prevents further motions and leads to deposition.

[30] 5. Diffusion, which is the random motion of sediment perpendicular to the flow. Diffusion disperses the grains and flattens the topography.

[31] In this preliminary work, transitions are extremely simplified in order to reduce the number of parameters. It is clear that more realistic (complete) sets of transitions should be implemented in the future to concentrate on different aspects of sediment transport: saltation, reptation, armoring. However, considering all the physical mechanisms together, transitions cannot be examined in isolation because only their combined and repeated actions are able to reproduce realistic sediment transport properties when averaged over space and time. For example, vertical deposition rates are the result of transitions associated with deposition and gravity. Similarly, sediment transport occurs only after a sequence of transitions that reproduce the initiation of movement (erosion), transport, and the end of movement (deposition).

[32] An important ingredient of the model is that each transition is characterized by a rate parameter with the dimension of a frequency. These transition rates introduce into the model the characteristic time scales of the physical mechanisms under consideration (Table 1). In practice, the whole process can be described as a generalized Poisson process (see Appendix B and *Narteau et al.* [2001]). Given a doublet transition from configuration u to v and the associated rate parameter Λ, the probability that a doublet in configuration u undergoes a transition toward configuration v in the infinitesimal time interval dt is Λdt; for n doublets in configuration u the probability to have one transition toward the configuration v in the infinitesimal time interval dt is $n\Lambda dt$. Extended to the entire population of doublets and all active transitions at a given time, the probability per unit of time to have a single transition is simply proportional to the sum of all the transition rates. In other word, the time delay before the next transition is inversely proportional to the sum of all the transition rates.

Table 1. Units and Values of the Parameters of the Model of Sediment Transport[a]

Variable	Description	Units	Values
	Elementary Units		
l_0	Length	$[L]$	
t_0	Time	$[T]$	
τ_0	Stress	$[M][L]^{-1}[T]^{-2}$	
	Model Parameters		
L	System width and length	l_0	[400, 600]
H	System height	l_0	100
Λ_0	Transition rate for erosion	$1/t_0$	1
Λ_t	Transition rate for transport	$1/t_0$	1.5
Λ_c	Transition rate for deposition	$1/t_0$	0.5
Λ_g	Transition rate for gravity	$1/t_0$	10^5
Λ_d	Transition rate for diffusion	$1/t_0$	0.01
a	Erosion/transport coefficient	1	0.1
b	Deposition coefficient	1	10
$\tau_2 - \tau_1$	Erosion range	τ_0	100

[a]Transition rates for erosion, deposition, and transport are chosen close to one with $\Lambda_c < \Lambda_0 < \Lambda_t$. Gravity (Stokes' law) and diffusion are occurring over much shorter and longer periods of time, respectively. We chose $\Lambda_c \ll \Lambda_0 \ll \Lambda_t$. Here $a < 1$ corresponds to the ratio between vertical and horizontal transition rates for erosion and transport and $b > 1$ corresponds to the ratio between deposition rates on flat and rough surfaces (see Figure 2).

Then, the main point in our algorithm is that at each iteration (i.e., time step) only one doublet (i.e., two cells) undergoes a transition from one configuration to another. The time step, the transition type, and the doublet that undergoes this transition are randomly chosen according to the present state of the system. This algorithm is therefore a time-dependent stochastic process whose current rate is given by the number of active transitions over time (i.e., the sum of all transition rates of active doublets).

[33] When the buildup of sediment exceeds the angle of repose, avalanches occur. These avalanches are introduced into the model via the dynamics of the *Bak et al.* [1988] sandpile model. If the height difference between two neighboring columns of sediment exceeds n_c cells, the highest sedimentary cells of the highest column are randomly redistributed onto the lower neighboring sites. As this redistribution alters the height differences, new redistributions of cells may occur, triggering a so-called cascade mechanism. As a result, a pile of sedimentary cells cannot have slopes steeper than a critical slope determined by the n_c value (see section A2).

[34] All boundary conditions are incorporated into the sediment transport model by using the following specific set of states and transitions:

[35] 1. A neutral state is used to construct solid boundaries. Cells in a neutral state do not interact with their neighborhood and they are not involved in any transition. For example, the solid bedrock on which the sediment is moving is a horizontal plane composed of neutral cells.

[36] 2. A removal state is used to introduce output fluxes of sediment. It requires at least one transition in which a sedimentary cell in contact with a removal cell is replaced by a fluid cell. Here, these removal states occur along the downwind border.

[37] 3. An injection state is used to introduce input fluxes of sediment. It requires at least one transition in which a fluid cell in contact with an injection cell is replaced by a sedimentary cell. Here, these injection states occur along the upwind border.

[38] Transitions involving removal/injection states are associated with different rates that control the intensity of output/input fluxes over time. Then, according to the orientations of these transitions, the magnitude of their transition rates, and the positions of neutral cells, we can accurately replicate almost any type of geometry and boundary condition.

3.2. A Lattice Gas Cellular Automaton Model

[39] Simultaneously with the evolution of the topography in the model of sediment transport, a lattice gas cellular automaton model is used to compute the flow [see *Hardy et al.*, 1976; *Frisch et al.*, 1986; *Chopard and Droz*, 1998; *Rothman and Zaleski*, 2004, and references therein]. This numerical method converts discrete motions of a finite number of fluid particles into physically meaningful quantities and offers an alternative to the full resolution of the Navier-Stokes equations. In addition, such a discrete model seems particularly useful to analyze bed form dynamics because it permits introduction of changing boundary conditions (i.e., the evolving topography) that are extremely difficult to tackle with conventional techniques implementing a set of differential equations.

[40] To reduce the computation time, we do not implement a 3-D LGCA. Instead, we consider a set of uniformly spaced vertical planes parallel to the direction of the flow (this spacing $\Delta_s = 5$ cells is a parameter of the model). Each plane is composed by the square lattice of the model of sediment transport (see section A1), and, confined to this plane, fluid particles can fly from cell to cell along the direction specified by their velocity vectors. Within this square lattice, we use a multispeed model taking into account motions of particles between nearest and next nearest neighbors [*d'Humières et al.*, 1986]: slow speed particles are moving between nearest neighbors, fast speed particles are moving between next nearest neighbors (Figure 3a). Two fluid particles cannot sit on the same site and interactions between particles take the form of local instantaneous collisions on sites with several particles (Figure 3b). Then, the evolution of the system during one iteration (or motion cycle) consists of two successive stages: a propagation phase during which particles move from their cells to their neighbors along the direction of their velocity vectors, and a collision phase during which particles on the same cell may exchange momentum according to the imposed collision rules (Figure 3b). These collision rules are chosen in order to conserve both mass and momentum.

[41] All boundary conditions of the flow are described in section C1. The most important for our interests is that fluid particles can move only within the fluid state of the cellular automaton of sediment transport. Other states are considered as boundaries on which the fluid particles are rebounding. Accordingly, motions of fluid particles adapt to changes in topography, and the flow field is strongly coupled to the bed form dynamics. In order to implement this feedback mechanism of the topography on the flow, we continuously monitor the evolution of the bed topography; the height of the interface between the sediment and the fluid. Thus, we can evaluate the direction of the normal to this topography, $\vec{n}$, and determine

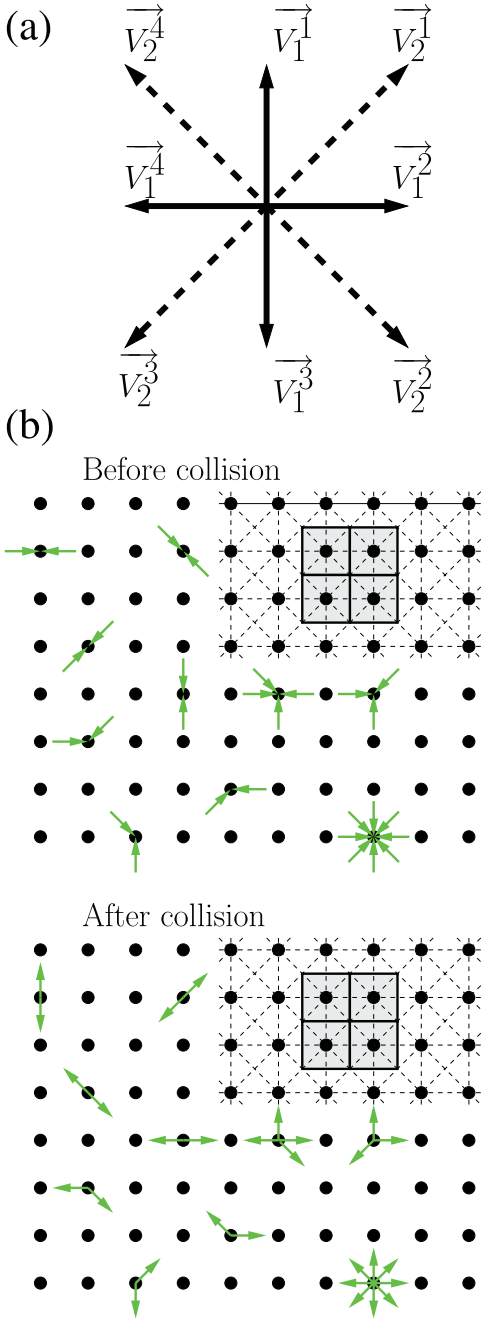

Figure 3. (a) The different velocity vectors in the lattice gas cellular automaton model. We have $\|V_2^i\| = \sqrt{2}\|V_1^i\|$. (b) Different examples of collisions between fluid particles (see the entire list by *d'Humières et al.* [1986]). Particles and their velocity vectors are represented by arrows. Each dot represents the nodes of the LGCA and the center of the cells of the model of sediment transport. In the top right, we show four of these cells in light gray and the connections along which the fluid particles are moving (dashed lines).

locally how a fluid particle rebounds on a sedimentary cell (see section C2).

[42] In order to determine both components of the local velocity vector in each plane of the LGCA, velocity vectors of fluid particles are averaged over $l_w \times l_w$ cells and t_w consecutive motion cycles (here $l_w = 5$ and $t_w = 50$). This averaging is necessary to reduce the statistical noise, but similar results can be obtained with different sets of parameters $\{l_w, t_w\}$. If necessary, between two planes of the LGCA, each component of the local velocity vector is linearly interpolated from adjacent values along lines perpendicular to these planes. The velocity field $\overrightarrow{V}$, expressed in terms of a number of fluid particles, and normal to topography is then used to calculate the bed shear stress

$$\tau_s = \tau_0 \frac{\partial \overrightarrow{V}}{\partial \overrightarrow{n}}, \tag{1}$$

where τ_0 is the stress scale of the model.

[43] Assuming a linear relation between bed shear stress and erosion rate, we consider that, in the model of sediment transport, the transition rate for erosion obeys the equation

$$\Lambda_e = \begin{cases} 0 & \text{for } \tau_s \le \tau_1 \\ \Lambda_0 \dfrac{\tau_s - \tau_1}{\tau_2 - \tau_1} & \text{for } \tau_1 \le \tau_s \le \tau_2 \\ \Lambda_0 & \text{else,} \end{cases} \tag{2}$$

where Λ_0 is a constant rate, τ_1 is the threshold for motion inception and τ_2 is a slope parameter ($\tau_s < \tau_2$). $(\tau_s - \tau_1)$ is the excess shear stress from which we can account for the feedback mechanism of the bed shear stress on the topography. During the numerical simulations, the only free parameter is τ_1, the lower threshold of erosion. All the other parameters of the model are kept constant including $(\tau_2 - \tau_1)$. Thus, we modify the excess shear stress and we can associate changes in the τ_1 value with variations in flow velocity: the higher the τ_1 value is, the lower the flow velocity is.

[44] Finally, the sediment transport and the LGCA are fully coupled via the rebounds of fluid particles on the sedimentary cells and the dependency of the erosion rate on the bed shear stress. As the density of sedimentary cells in motion is mainly controlled by the intensity of the erosion process, the flow also has an influence on transport and deposition processes. However, injecting more complete, but more complicated, feedback mechanisms is already possible, and, in the future, the flow properties (i.e., τ_s) can also play a role in altering the transition rates for transport, deposition and diffusion.

[45] In practice, the numerical simulations consist of rapid switching between the model of sediment transport and the LGCA (see Appendix D). In fact, we estimate the frequency at which the motion cycles of the LGCA should occur from the transition rates of erosion and deposition (Table 1) Thus, the flow is recalculated over time scales much shorter than the characteristic time required to move an individual sedimentary cell, and we compute the simultaneous evolution of topography and bed shear stress.

4. Typical Dune Patterns of the Cellular Automaton Model

[46] In the model of sediment transport, all parameter units are expressed in terms of l_0, the elementary length of the cellular automaton, and $t_0 = 1/\Lambda_0$, the time scale for erosion (Table 1). We assume the transition rates for deposition and transport are slightly lower and higher,

respectively, than the transition rate for erosion. Thus, there are always sedimentary cells in motion. As the transition rate for gravity is determined from the Stokes velocity, it is a few orders of magnitude larger than all the other transition rates. In contrast, the transition rate for diffusion is a few orders of magnitude smaller. In all the computations presented here, these various parameters are held constant. A systematic and quantitative analysis of the dune instability over the entire parameter space is planned in future work. We note, however, that initial tests show that the qualitative pattern does not change when parameter values are varied over an order of magnitude.

[47] The characteristic length and time scales $\{l_0, t_0\}$ are discussed in section 5 from the linear stability analysis of a flat sediment bed and comparisons between observations and model outputs. In this section, we present some distinctive morphological features of the model which are particularly relevant to this objective. A more complete description of the morphology of basic dune types generated by the model (i.e., barchan, linear and transverse dunes) as well as the influence of the bed shear stress on the dynamics of these dunes are analyzed in more detail in the future.

[48] Figure 4a shows the evolution of a square pile of sediment from $t/t_0 = 0$ to $t/t_0 = 3800$. In order to ensure mass conservation, each sedimentary cell ejected from the system in the direction of the flow is reinjected randomly through the opposite boundary. Over a short time, from the transient growth of some perturbations, secondary structures appear and propagate on the flat surface at the top of the pile. Smaller structures being faster, they rapidly merge with larger ones to form superimposed transverse dunes. Meanwhile, the face oriented against the direction of the flow is accumulating all the sediment that is uniformly reinjected in the system. As a consequence, this face is continuously growing in height and the recirculation bubble is continuously increasing in length. Downstream of the highest zone of the dune, bed shear stress and sediment flux are much lower than on the side of the dune, and the superimposed transverse dune form horns, along which are concentrated most of the output sand fluxes. The face against the flow continues to grow until it entirely covers the initial pile of sediment. Simultaneously, horns grow from both sides of the dune, ejecting smaller dunes at regular time intervals. As this evolution proceeds, the structure moves in the direction of the flow and its shape converges toward a quasi-stationary equilibrium state which is commonly described as a crescentic barchan dune.

[49] Dynamically, a typical feature of this barchan dune is the systematic occurrence of secondary structures on the surface of the dune. These superimposed bed forms nucleate at a constant rate on the face exposed to the flow. Then, they propagate and can grow by merging until they collapse when they reach the slip face of the major dune. Along transect lines parallel to the flow, the distance between two successive slip faces is almost constant and a characteristic wavelength of about 40 l_0 is measured at different times. Not surprisingly, this is approximately the same wavelength as for the oscillations observed on the flat surface at the top of the initial sand pile.

[50] Superimposed bed forms are distinct features that can be observed across almost all types of dunes (Figure 1). In the model, this is also the case, and Figure 4b illustrates how secondary structures nucleate and propagate over transverse dunes. In these numerical simulations, we use periodic boundary conditions in horizontal directions and the initial condition is a flat and thick layer of sedimentary cells. During the first phase, the destabilization of the flat layer of sediment, we observe the formation of small transverse dunes with a characteristic wavelength of about 40 l_0. These transverse dunes are growing by merging until they reach a characteristic length of about 80 l_0. During this growth phase, the number of terminations decreases and the density of secondary dune patterns on the faces exposed to the flow is almost always the same. These superimposed structures destabilize the dunes and generate defects from which terminations may appear or migrate from one dune to another.

[51] The similarities between the elevation profile and bed shear stress indicate unambiguously that, in the model, these two parameters are highly coupled with one another (Figures 4c and 4d). This is true at the length scale of the dune but also for the superimposed bed forms at smaller length scales. Most of the time, it is even easier to distinguish topographic irregularities from the stress field. For example, small waveforms in the bed elevation profile across a transverse dune field (Figure 4c) correspond to similar but larger oscillations of the bed shear stress (Figure 4d). In both cases, the oscillation has a wavelength of approximately 40 l_0.

[52] In the model, the superimposed dune patterns that are observed across barchan and transverse dunes are similar in many respects. More interestingly, there are also similarities in the destabilization of a flat sediment layer and the nucleation of superimposed structures. All these indices suggest that similar processes are operating during the nucleation of dunes and their destabilization by secondary bed forms. Consequently, the characteristic length scale for the formation of these structures give us the opportunity to set the characteristic length and time scales of the model from field observations (Figure 1).

5. Setting the Length and Time Scales of the Model

[53] In this cellular automaton approach, the macroscopic properties of sand transport result from the interactions between the elements of the system over time, and they cannot be derived analytically from the parameterization of the model. To set the length and time scales of the model, we run the model under specific conditions.

5.1. Linear Stability Analysis of a Flat Sand Bed

[54] As discussed in section 2, the standard tool to investigate the properties of an instability is to perform the linear stability analysis. In order to compute the dispersion relation $\sigma(\lambda)$ in our model, we generate an entire range of bed elevation profiles by superimposing sinusoidal waves of wavelength λ and vanishing amplitude A onto a flat sand bed (Figure 5). Above these beds, we stabilize the flow and, when a quasi-stationary equilibrium state is reached, at $t = 0$, we start the model of sediment transport. Then, at regular time intervals, we estimate the amplitude and the mean wavelength of the bed profile from the autocorrelation function (see caption of Figure 5). For all wavelengths, we

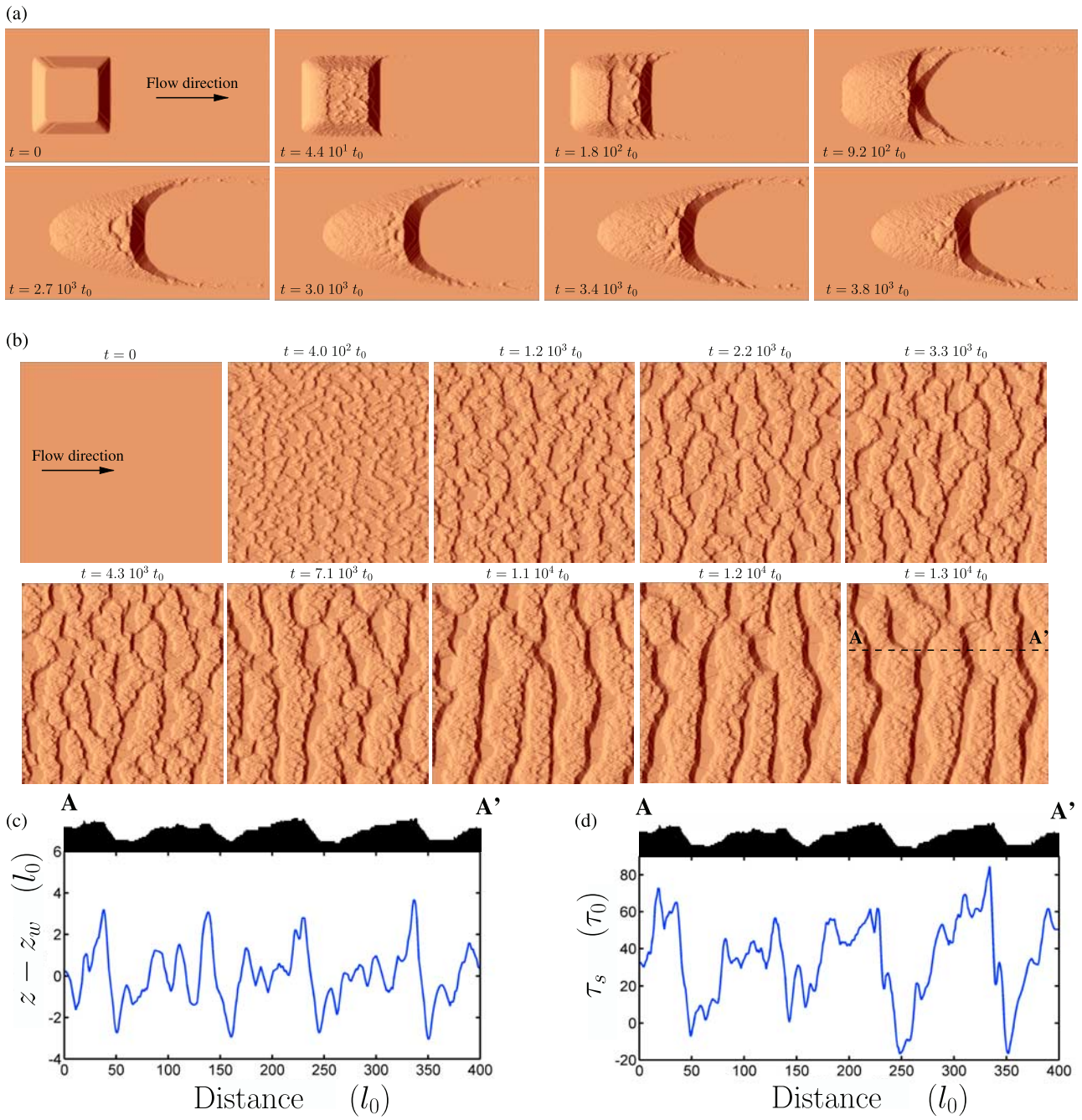

Figure 4. (a) Evolution of a square sand pile until a crescentic barchan shape reaches a quasi-stationary equilibrium state ($H = 100\ l_0$, $L = 600\ l_0$). (b) Formation of a transverse dune field until it reaches a quasi-stationary equilibrium state ($H = 100\ l_0$, $L = 400\ l_0$). The average number of dunes, defects, and terminations are almost constant despite some random fluctuations. In Figures 4a and 4b, $\tau_1 = 20\ \tau_0$. Note the characteristic length scales for the nucleation of dunes over short time and the formation of secondary bed forms over long time. (c) Along a transect line parallel to the direction of the flow (see AA' in Figure 4b), the difference between the elevation z and the local mean elevation z_w averaged over a sliding window of length 40 l_0. (d) The bed shear stress at the solid fluid interface along the same transect line. In Figures 4c and 4d, the elevation profile is shown in black at the top of the graph.

estimate the time period over which the initial wavelength of the perturbation remains unchanged. During this time period, we verify that the growth in amplitude is consistent with an exponential function, and, from the best-fit solution we estimate the growth rate (Figure 5).

[55] Figure 6 shows the magnitude of the growth rate $\sigma(k)$ with respect to the wave number $k = 2\pi/\lambda$ for three different τ_1 values. They all exhibit the same general shape, with a positive region for a finite range $0 < k < k_c$ and a negative one for $k > k_c$. Furthermore, one can identify a clear maximum corresponding to the fastest growing mode

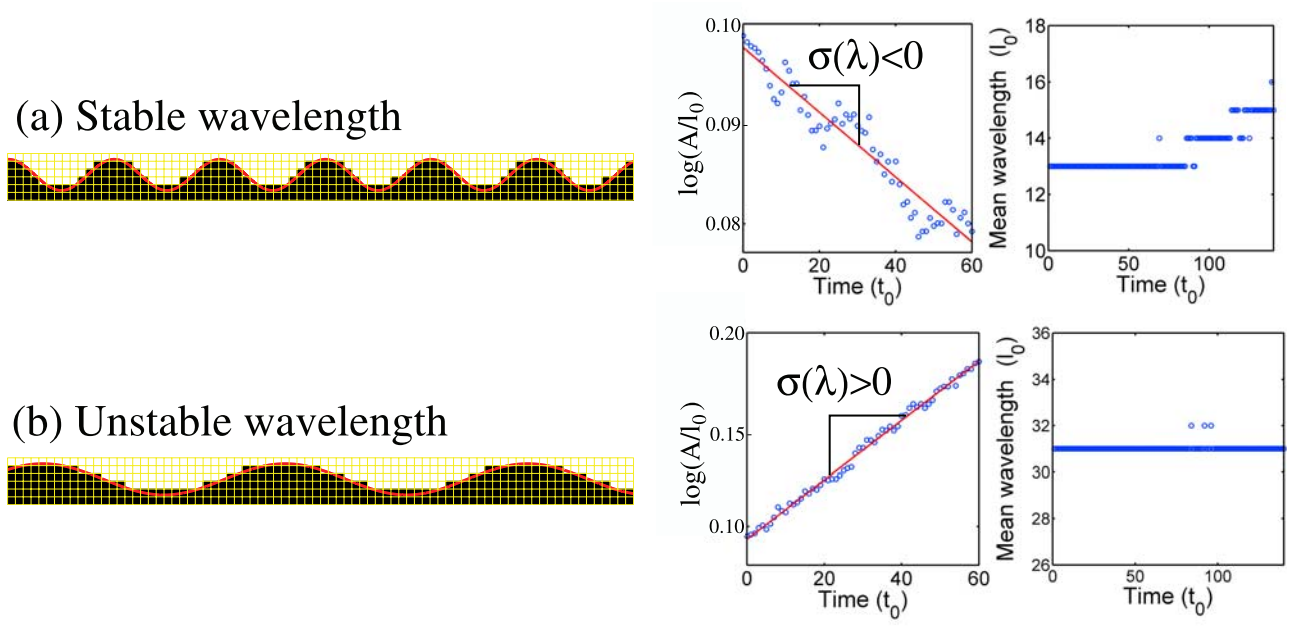

Figure 5. Linear stability analysis in the model with examples of (a) stable and (b) unstable wavelengths. As shown on the left, the initial condition at $t = 0$ is a flat sand bed disturbed by a sinusoidal wave of wavelength λ ($\lambda = 13\ l_0$ (Figure 5a); $\lambda = 31\ l_0$ (Figure 5b)). The solid line is the continuous profile from which the initial bed profile $h(\lambda, x, 0)$ has been discretized. The autocorrelation function of the bed profile $C(\lambda, l, t) = \langle h(\lambda, x, t)h(\lambda, x + l, t)\rangle - \langle h(\lambda, x, t)\rangle^2$ gives the amplitude $A(\lambda, t) = 2\sqrt{2C(\lambda, 0, t)}$ and the mean wavelength (the position of the first peak). Assuming a linear regime, $A(\lambda, t)$ is fitted by a exponential function of the form $\exp(\sigma(\lambda)t)$ during the period over which the mean wavelength remains unchanged. If $\sigma(\lambda) > 0$, the wavelength is unstable and the pattern is growing; if $\sigma(\lambda) < 0$, the wavelength is stable and the pattern is decaying. The most unstable wavelength λ_{max} is the wavelength at which $\sigma(\lambda)$ reaches a maximum.

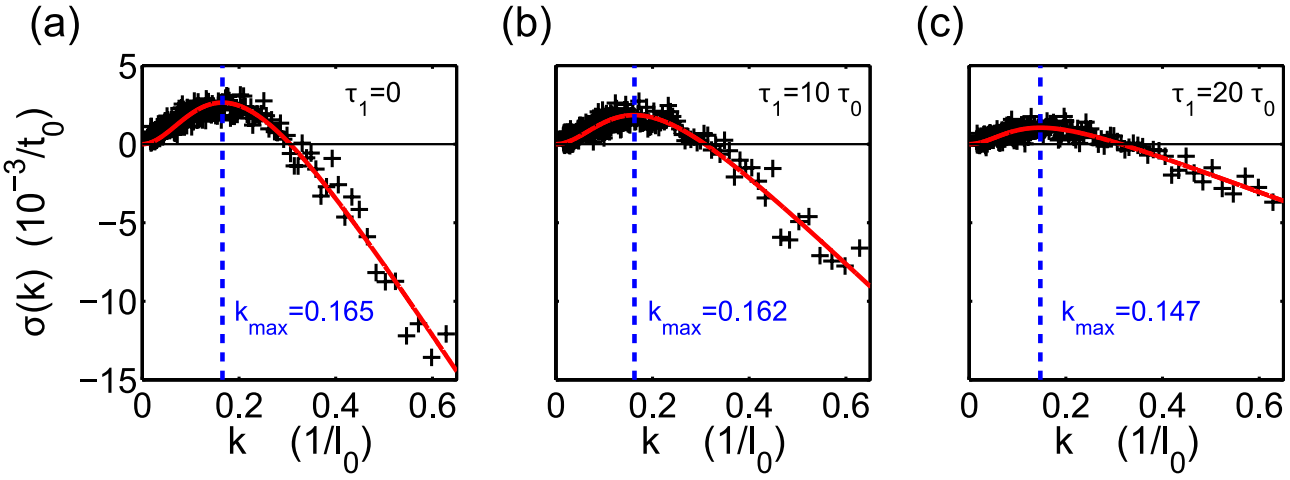

Figure 6. Results of the linear stability analysis for (a) $\tau_1 = 0$, (b) $\tau_1 = 10\ \tau_0$, and (c) $\tau_1 = 20\ \tau_0$. Crosses are the estimated growth rates as a function of the disturbance wave number $k = 2\pi/\lambda$ for wavelength in the range $10\ l_0 < \lambda < 385\ l_0$ by steps of $0.5\ l_0$. The red curve is the best fit of these data using equation (3). The set of adjustable parameters $\{\sigma_0, \alpha, \beta\}$ is $\{14\ 10^{-3}\ t_0^{-1}, 0.65, 5.0\}$ (Figure 6a), $\{8.8\ 10^{-3}\ t_0^{-1}, 0.59, 5.5\}$ (Figure 6b), and $\{3.5\ 10^{-3}\ t_0^{-1}, 0.41, 7.6\}$ (Figure 6c). The dashed line shows the position of the fastest growing mode $k_{max} = 2\pi/\lambda_{max}$.

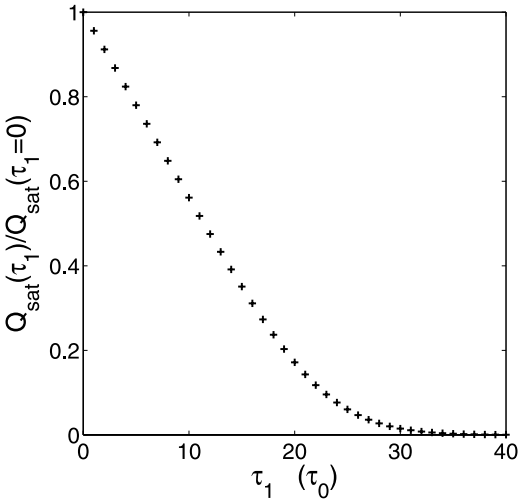

Figure 7. The saturated flux with respect to the τ_1 value. $Q_{sat}(\tau_1)$ is normalized by its value $Q_{sat}(\tau_1 = 0)$. Note that an increasing τ_1 value corresponds to a decreasing flow strength.

$k_{max} = 2\pi/\lambda_{max}$, which gives therefore the characteristic wavelength for the formation of dunes on a flat sand bed. To quantify this fastest growing mode, we fit our data points to the function

$$\sigma(k) = \sigma_0(\alpha k)^2 \frac{1-\beta(\alpha k)}{1+(\alpha k)^2}, \tag{3}$$

which is the analytical expression of the growth rate proposed by *Andreotti et al.* [2002] (see also *Claudin and Andreotti* [2006]; Fourrière et al. (submitted manuscript, 2009b)). Using this equation, the three fitting parameters $\{\sigma_0, \alpha, \beta\}$ are determined by a nonlinear least squares fitting procedure.

[56] From the best-fit solution shown in Figure 6, we observe that the exact position of the maximum depends of the τ_1 value: λ_{max} is decreasing for an increasing wind strength (see discussion in section 6). Nevertheless, we approximately get $\lambda_{max} = 2\pi/k_{max} \approx 40\ l_0$. Interestingly, this value is very close to the characteristic length of secondary bed forms in Figures 4a and 4b. More importantly, the λ_{max} value will be the key point of the scaling relation between the dunes in the model and those in the field.

[57] Figure 6 also shows that equation (3) fits the data points equally well for a wide range of τ_1 values. Then, in addition to the determination of the maximum growth rate, it is possible to use equation (3) to interpret the values of the three fitting parameters $\{\sigma_0, \alpha, \beta\}$ with respect to continuous models for sand transport and dunes [*Andreotti et al.*, 2002] As a matter of fact, σ_0 is proportional to the input sand flux, β encodes hydrodynamics effects that determine variations of the flow velocity above the elevation profile [*Jackson and Hunt*, 1975; Fourrière et al., submitted manuscript, 2009a] and α is related to the saturation length l_{sat} of the sand flux. From the amplitude of the dispersion relation, we consistently observe, for instance, that the σ_0 value is decreasing with an increasing τ_1 value (i.e., a decreasing flow strength).

5.2. Saturation Length and Flux

[58] Because of the negative feedback of the moving grains on the flow, a wind of a given strength can only transport a limited amount of sediment. Furthermore, transport is observed only if the shear stress τ_s applied by the fluid on the bed is above a threshold τ_c. As a consequence, generic transport laws are of the form

$$Q_{sat} = \begin{cases} 0 & \text{if } \tau_s \le \tau_c \\ \tau_s^{\gamma}(\tau_s - \tau_c) & \text{if } \tau_s \ge \tau_c, \end{cases} \tag{4}$$

where γ is a positive (or null) constant [*Bagnold*, 1956; *Anderson and Haff*, 1988; *Ungar and Haff*, 1987; *Rasmussen et al.*, 1996; *Andreotti*, 2004]. In our model, we can directly compute this saturation flux on a flat sand bed, and Figure 7 shows how the Q_{sat} value is decreasing with respect to a decreasing flow strength (i.e., an increasing τ_1 value). In addition to this direct measurement, the exact relation can be derived from equation (2), an expression which can be changed in the future to adapt to various transport laws.

[59] As described in section 2, the space lag l_{sat} between the actual flux and its saturated value can be modeled by a first-order relaxation which can be expressed as

$$\partial_x q \sim \frac{Q_{sat} - q}{l_{sat}}. \tag{5}$$

This saturation length can also be extracted from the linear stability analysis because, in equation (3), $\alpha = l_{sat}/l_0$. As shown in the caption of Figure 6, the best-fit value of the parameter α indicates that $l_{sat} \approx 6\ l_0$ with a slight tendency to decrease with increasing flow strength.

[60] In order to check consistency, we use our model to perform a direct calculations of this saturation length, and we consider a numerical setup which is directly inspired from experimental data [*Bagnold*, 1941; *Elbelrhiti et al.*, 2005; Andreotti et al., submitted manuscript, 2009]. Indeed, in these simulations, the initial condition is characterized by a transition from a flat bedrock to a flat sand bed close to the boundary across which the flow is injected (Figure 8a). In addition, the boundary conditions are such that sand flux is null above the bedrock. Then, for a given flow strength (i.e., τ_1 value), we calculate the sand flux above the sand bed and along the direction of the flow. Then, over short time, we estimate how the sand flux changes from zero to its equilibrium value. Figure 8b show these calculations for $\tau_1 = 0$ (symbol). We then fit to these points using an exponential law of the form $q/Q_{sat} = 1 - \exp(-(x - x_0)/l_{sat})$, which is the solution of equation (5). The best fit gives $l_{sat} = 6.9\ l_0$, a value which is in good agreement with the α values that have been obtained in the linear stability analysis from the fit of the dispersion relations (Figure 6).

5.3. Characteristic Length and Time Scales of the Model

[61] We are now ready to set the characteristic length and time scales of our model. *Elbelrhiti et al.* [2005] have shown that the windward slope and the flanks of barchans behave as flat beds and generically show superimposed bed forms as soon as they are large enough. The analysis of the

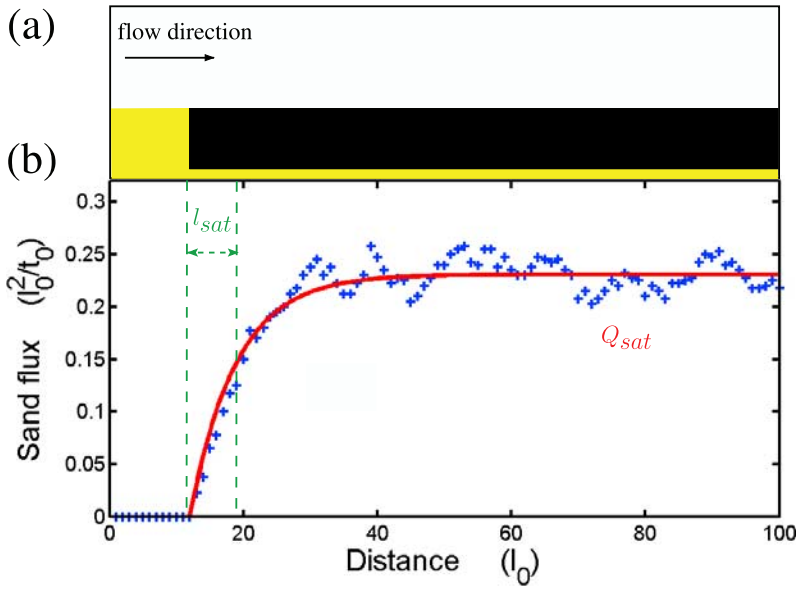

Figure 8. Estimations of saturation length and saturated flux in the model for $\tau_1 = 0$. (a) Initial condition of the model of sediment transport; close to the boundary across which the flow is injected there is a transition from a flat bedrock to a flat sand bed located at $x_0 = 12\ l_0$. (b) Sand flux over a short time period along the direction of the flow (crosses) and best exponential fit to these data in relation to equation (5) (see text). The fit gives $Q_{\mathrm{sat}} = 0.23\ l_o^2/t_0$ and $l_{\mathrm{sat}} = 6.9\ l_0$.

wavelength distribution of these secondary structures gives a characteristics value on the order of 20 m. This value is not specific to the Atlantic Sahara where these measurements were performed. Except in some places where the wind hardly exceeds the transport threshold (Andreotti et al., submitted manuscript, 2009), it is rather typical and may be representative of the smallest bed forms in dune fields. Following the linear stability analysis, we can then associate this length scale with $\lambda_{\max}$. As we found $\lambda_{\max} \approx 40\ l_0$ in the model, we must therefore set in our cellular automaton approach

$$l_0 \approx 0.5\mathrm{m}. \tag{6}$$

It is important to emphasize that this value depends on the specific $\lambda_{\max}$ values estimated in our model and observed in nature. As these values may vary within the entire parameter space of the model and in different types of natural environments [*Claudin and Andreotti*, 2006], an l_0 value of 0.5 m does not have any kind of generality and should not be considered as a definitive value for this CA dune model.

[62] From the elementary length scale l_0, it is now possible to set the characteristic time scale t_0. One more time, we achieve this with respect to experimental observations, and more precisely from the relationship between the wind velocity and the saturated flux. First, from equation (4), it is possible to compute the ratio between the saturated flux Q_{sat} and its value Q^0_{sat} for $\tau_{\mathrm{c}} = 0$. Introducing the shear velocity $u^* \equiv \tau_s^{1/2}$, we get

$$\frac{Q_{\mathrm{sat}}}{Q^0_{\mathrm{sat}}} = 1 - \left(\frac{u_{\mathrm{c}}}{u_*}\right)^2. \tag{7}$$

Wind velocity time series allow us to compute the average value $\langle u_*/u_{\mathrm{c}} \rangle$, which would correspond to a constant wind strength producing the same sediment flux. From this shear velocity ratio, we can compute the value of $Q_{\mathrm{sat}}/Q^0_{\mathrm{sat}}$ with equation (7). Consistently, we choose the same value for $Q_{\mathrm{sat}}(\tau_1)/Q_{\mathrm{sat}}$ ($\tau_1 = 0$). Then, from Figure 7 we can read the corresponding τ_1 value. Finally, matching the average saturated flux in the model to that in the dune field, we get

$$t_0 = \frac{Q_{\mathrm{sat}}(\tau_1)}{\langle Q_{\mathrm{sat}} \rangle} l_0^2. \tag{8}$$

In this formula, $Q_{\mathrm{sat}}(\tau_1)$ is the saturated flux in the model, measured in units of t_0 and l_0, and $\langle Q_{\mathrm{sat}} \rangle$ is the saturated sand flux measured from the wind data.

[63] For example, in the Atlantic Sahara (Figure 1d), the wind data give $\langle u_*/u_c \rangle \approx 1.6$ and $\langle Q_{\mathrm{sat}} \rangle \approx 100$ m^2 a [*Elbelrhiti et al.*, 2005] and we obtain $\tau_1 \approx 9\ \tau_0$. Inversely, for $\tau_1 = 20\ \tau_0$, the value used for the numerical simulations shown in Figure 4, we obtain $\langle u_*/u_c \rangle \approx 1.1$. For grains of 180 μm such as those of the desert in Atlantic Sahara, this ratio corresponds to $\langle Q_{\mathrm{sat}} \rangle \approx 12.5$ m^2 a [*Andreotti*, 2004]. Then, equation (8) gives $t_0 \approx 7.8 \times 10^{-4}$ a and the simulations shown in Figures 4a and 4b last for 3 and 11 years, respectively.

6. Conclusion and Perspectives

[64] We propose a new model for bed form dynamics, which relies on couplings between a cellular automaton for sediment transport and a lattice gas cellular automaton for flow dynamics. By construction, this model allows independent investigations of the different types of transport, erosion and deposition processes. Here, we focus on the

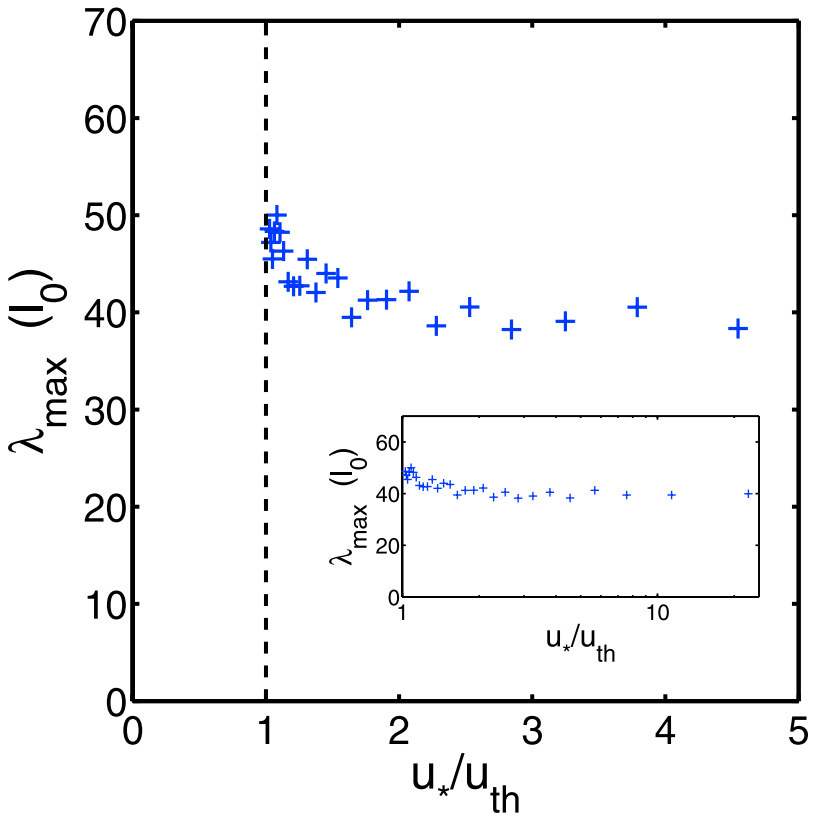

Figure 9. Evolution of the most unstable wavelength with respect to the flow velocity dimensionalized by the threshold velocity for sediment transport. The inset shows a wider range of velocity in a logarithmic scale. Note the well-defined plateau when $u_*/u_c \to \infty$.

hydrodynamic instability induced by the relationship between the bed shear stress and the topography.

[65] From observations of our numerical dune fields and a linear stability analysis, we have clearly identified a characteristic length scale λ_{max} for the formation of dunes in the model. The same instability is also responsible for the nucleation of secondary bed forms and their propagation on faces of dunes exposed to the flow. From comparisons with dune field measurements, we deduce a unit length scale l_0 for our discrete model. Not surprisingly, this length scale is few times lower than the saturation length l_{sat}, the relevant length scale for dunes.

[66] The discussion of scale setting in section 5.3 was implicitly based on a fixed value $\lambda_{max} \approx 40\ l_0$. However, as shown in Figure 6, the position of the maximum growth rate depends on the τ_1 value. Recalling that this parameter encodes the value of the ratio u_*/u_c, we can compute the wavelength of the most unstable mode as a function of the wind strength, which is displayed in Figure 9. λ_{max} has a gentle trend to decrease with u_*/u_c, and reaches a plateau at the value 40 l_0 as soon as the velocity ratio is around 1.5. This general decreasing trend is in agreement with recent studies [*Parteli et al.*, 2007a, 2007b; *Andreotti and Claudin*, 2007; Andreotti et al., submitted manuscript, 2009]. Nevertheless, further investigation is needed to attribute this behavior to a precise mechanism in the model.

[67] In this cellular automaton approach, the ratio λ_{max}/l_{sat} between the characteristic length scale for the formation of dunes and the saturation length is on the order of 6.5. This value is less by a factor of 3 than what we estimated from field and experimental measurements (Andreotti et al., submitted manuscript, 2009). Similarly, the value for the fitting parameter β in the dispersion relation (equation (3)) is off by a factor of 4 in comparison with what we can compute within a complete hydrodynamical model (Fourrière et al., submitted manuscript, 2009a). These quantitative discrepancies may be partly attributable to the simple linear closure (see equation (2)) that we have taken to relate the basal shear stress to the velocity gradient. This relation could be replaced by a more sophisticated function that better describes the turbulent nature of the flow above a rough topography.

[68] Sediment transport and the subsequent presence of bed forms are observed on different planetary bodies (e.g., Earth, Mars, Titan), under water, in dry deserts as well as in Antarctica [*Claudin and Andreotti*, 2006, and references therein]). In these different cases, the characteristic time and length scales associated with these bed forms can change by a few orders of magnitude, because of the different values of the relevant parameters, in particular fluid and sediment densities and grain size. However, we expect that some of these bed forms may be the result of the same instability mechanism [*Claudin and Andreotti*, 2006]. This means for example that, with respect to additional physical mechanisms related to specific environmental features, our model can be directly used to analyze dune fields on Earth and

Mars. The only modification needed is the setting of the length and time scales $\{l_0, t_0\}$ to the correct values.

[69] In all natural environments where the dune instability can be observed, our discrete model may therefore be a useful tool to quantify sediment fluxes. Most importantly, it retains all the advantages of discrete models in analyzing pattern formation, but also exhibits, with respect to the flow, the instability mechanism which is likely to govern the development of dune patterns and the nucleation of secondary bed forms as well as the selection of dune sizes (section 2). Hence, it has to be developed to study a population of dunes and its stability under rotating wind conditions and fluctuating wind strength.

[70] Our cellular automaton is 3-D and can therefore be used not only to describe surface processes, but also the internal sedimentary structure of the dunes [*Bristow et al.*, 2000, 2007]. In the future, these structures can be examined (1) to test different scenarios for the formation of dunes, (2) to determine accumulation features in the presence of secondary bed forms and also (3) to analyze the effect of collisions between dunes.

[71] Finally, with our model, we establish a link between cellular automaton methods and continuum mechanics in such a way that we will be able to constrain structural complexity of dune fields by a set of well-defined physical quantities. We believe that the discontinuous nature of our model and the feedback mechanisms between topography and bed shear stress will allow this system to capture in more detail some of the most distinctive features of the evolution of complex dune fields in various natural environments.

Appendix A: Geometric Considerations

A1. Regular Lattices

[72] We use a 3-D cellular automaton model for sediment transport and a LGCA to compute the flow and quantify the bed shear stress. Therefore there are two independent lattices that need to be merged together. In the model of sediment transport we have parameterized the aspect ratio between height and length. As given by *Baas and Nield* [2007], an elementary cell has a square base of length l_0 and a height h_0. By definition, $l_0 \geq h_0$ and the adjustable aspect ratio $\eta = l_0/h_0$ has to be an integer for the coupling between the model of sediment transport and the LGCA. If $\eta = 1$, the elementary cell has a cubic shape; if $\eta > 1$, the elementary cell has a slab shape as in classical cellular automatons for dune dynamics [*Werner*, 1995]. Thus, the 3-D lattice of cells can be decomposed into 2-D horizontal square lattices and 2-D vertical rectangular lattices.

[73] In the LGCA, the collision rules conserve both mass and momentum in such a way that the velocities of fluid particles have to be the same in perpendicular directions (see section 3.2). For this reason, motions of fluid particles are implemented on regular square lattices. These square lattices have to fit perfectly into the vertical rectangular lattices of the model of sediment transport. Hence, each cell of the model of sediment transport is vertically and horizontally decomposed into ν and $\nu\eta$ cells of the LGCA (see example in Figure A1). The positive integer ν is a parameter of the model that determines the edge length of one cell of the LGCA (i.e., h_0/ν).

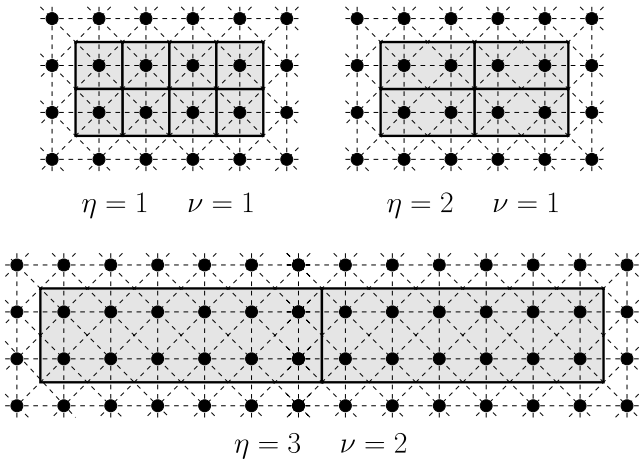

Figure A1. Examples of the overlapping lattices for different η and ν values. Gray cells represent elementary structures of the model of sediment transport; black dots and dashed lines represent the lattice nodes and the possible trajectories of fluid particles in the LGCA, respectively.

[74] Larger ν and η values allow for the modeling of smaller structures of the flow but require a longer computation time. Here, we take $\eta = \nu = 1$ for numerical efficiency. In this case, the two lattices overlap perfectly (see Figure 3), and elementary cells in both models have a similar square shape with an edge length l_0.

A2. Angle of Repose

[75] The angle of repose Θ of the granular material that forms our sediment layer is determined with respect to a critical height difference between two neighboring piles of sediment. This height can be expressed as a number of slabs n_c and we have

$$\tan\Theta = n_c \frac{h_0}{l_0} = \frac{n_c}{\eta}. \tag{A1}$$

Most of the time, because of the discrete nature of the system, it is necessary to choose the nearest positive integer to determine the n_c value. This is for example the case here when we choose $n_c = 1$ from $\eta = 1$ and $\Theta = 34°$ (the angle of repose of dry sand). Unfortunately, it gives an apparent angle of repose of 45°. To simulate more realistic angles of repose in the future, one solution is to approach the critical slope with integer values of η and n_c (e.g., $\tan(34°) \approx 2/3 \Leftrightarrow n_c = 2$ and $\eta = 3$, see section A1). However, there are always 3-D artifacts in discrete methods that calculate height differences between nearest or next nearest neighbors.

Appendix B: Algorithm of the Model for Sediment Transport

[76] All transitions of doublets occur sequentially over time according to the present configuration of doublets across the entire system (Figure B1). Thus, the system dynamics can be regarded as a Markov chain, a time-dependent stochastic process without memory. Practically, the whole process is defined in terms of a Poisson process.

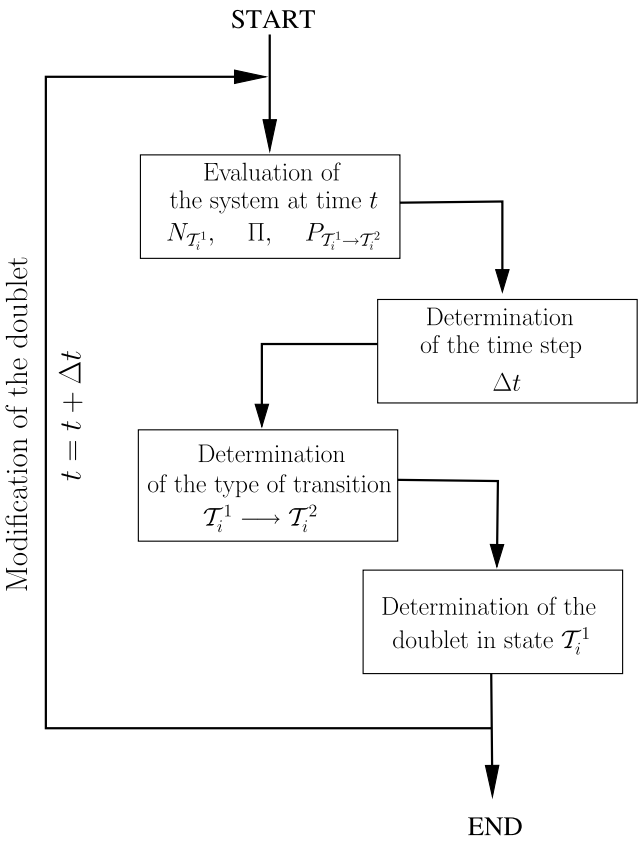

Figure B1. The algorithm of the model. $N_{\mathcal{T}_i^1}$ is the number of doublets in the configuration $\mathcal{T}_i^1$, $P_{\mathcal{T}_i^1 \to \mathcal{T}_i^2}$ is the probability for a transition from $\mathcal{T}_i^1$ to $\mathcal{T}_i^2$ to occur during the next time step Δt, and Π is the total transition rate of the system. At each iteration, or time step, a single doublet (i.e., two cells) changes its configuration. The time step, the transition type, and the doublet are successively chosen according to the present state of the system and three random numbers (see text).

This is not only an extremely common distribution observed in nature (i.e., exponential distribution of interevent times), this is also the simplest, as it only depends on one rate parameter. In addition, it possesses the elegant and useful additive property: the sum of two independent Poisson random variables with rates Λ_1 and Λ_2 is also a Poisson random variable with rate $\Lambda_1 + \Lambda_2$.

[77] Let us consider that we have ϑ active transitions. An active transition $i \in [1, \vartheta]$ is notated $\mathcal{T}_i$, and $\mathcal{T}_i^1$ and $\mathcal{T}_i^2$ are the initial and the final configurations of the doublet; $\Lambda_{\mathcal{T}_i^1 \to \mathcal{T}_i^2}$ is the transition rate associated with such a transition. $N_{\mathcal{T}_i^1}$ is the number of doublets in the configuration $\mathcal{T}_i^1$ and

$$N_{\mathcal{T}} = \sum_{i=1}^{\vartheta} N_{\mathcal{T}_i^1} \tag{B1}$$

is the total number of active transitions.

[78] For each active doublet in the configuration $\mathcal{T}_i^1$, the occurrence of the transition $\mathcal{T}_i$ obeys the Poisson distribution. Then, the waiting time t_t for this transition to occur is given by an exponential distribution characterized by a unique rate parameter $\Lambda_{\mathcal{T}_i^1 \to \mathcal{T}_i^2}$

$$P(t_t > \Delta t) = \exp\left(-\Lambda_{\mathcal{T}_i^1 \to \mathcal{T}_i^2} \Delta t\right). \tag{B2}$$

Generalizing the Poisson process to a population of active doublets, the distribution of the waiting times t_t until the next transition is given by

$$P(t_t > \Delta t) = \exp(-\Pi \Delta t), \tag{B3}$$

where

$$\Pi = \sum_{i=1}^{N_{\mathcal{T}}} N_{\mathcal{T}_i^1} \Lambda_{\mathcal{T}_i^1 \to \mathcal{T}_i^2} \tag{B4}$$

is the total transition rate of the system.

[79] For a given doublet configuration at time t, we first evaluate the number of doublets $N_{\mathcal{T}_i^1}(t)$ that can potentially change their configuration. Then, we calculate $\Pi(t)$ the total transition rate of the system. At each iteration only one doublet undergoes a transition to a new configuration. The time step Δt is therefore variable depending on the magnitude of $\Pi(t)$ (see equation (B4)). In practice, we draw at random a value r_1 between 0 and 1, and we consider that the waiting time for the next transition to occur is

$$\Delta t(t) = -\frac{1}{\Pi(t)} \ln(r_1). \tag{B5}$$

During this time step, the transition that occurs is also randomly chosen with respect to a weighted probability determined from

$$P_{\mathcal{T}_i^1 \to \mathcal{T}_i^2}(t) = \frac{N_{\mathcal{T}_i^1}(t) \Lambda_{\mathcal{T}_i^1 \to \mathcal{T}_i^2}}{\Pi(t)}. \tag{B6}$$

Numerically, we define a discrete cumulative distribution function for which steps are proportional to the values of $P_{\mathcal{T}_i^1 \to \mathcal{T}_i^2}(t)$. Then, we draw at random a value r_2 between 0 and 1. This value is associated with a step of the cumulative distribution function which determines in turn the type of transition that occur. Thus, transitions with the highest rates have more chance to be selected but transitions with small rates may also occur. Finally, when the transition i is selected, we draw at random an integer between 0 and $N_{\mathcal{T}_i^1}(t)$ in order to identify the unique doublet that undergoes this transition. Repeated a large number of times, such a procedure permits the continuous monitoring of the bed form dynamics.

Appendix C: Properties of the LGCA

C1. Boundary Conditions

[80] In all computations, fluid particles are vertically confined between the sediment layer lying on flat bedrock and a flat ceiling. This confinement prevents dissipation of momentum by keeping the number of fluid particles con-

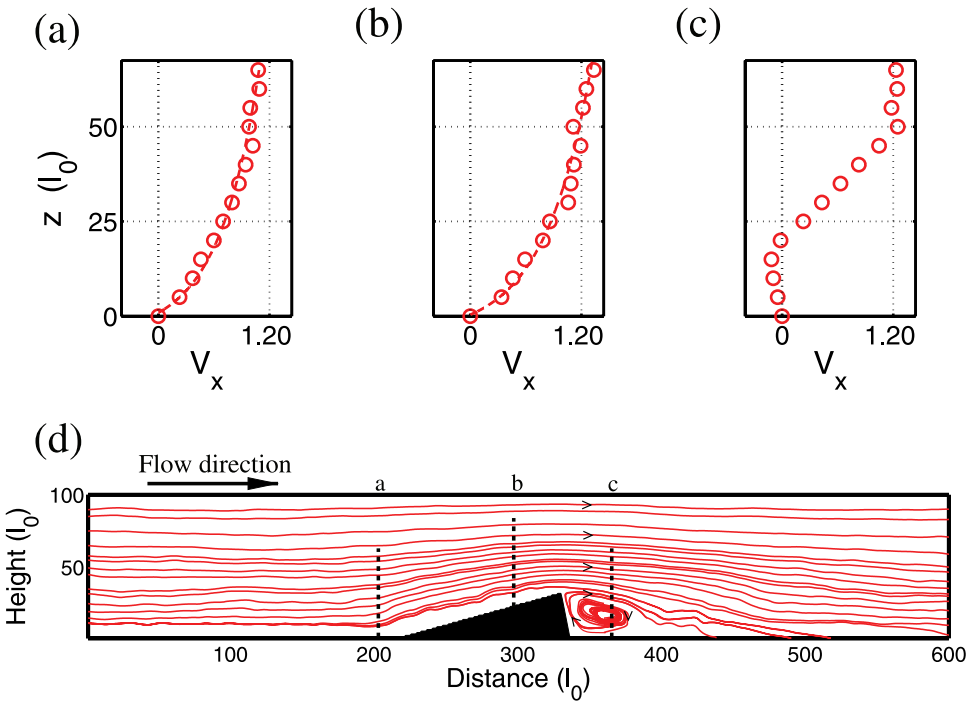

Figure C1. Velocity profiles (a) before, (b) on the slope, and (c) downwind of a dune. Note the free slip boundary condition along the ceiling, the logarithmic velocity profile before the crest and dune (the dashed line in Figures C1a and C1b), and the reverse flow in the recirculation zone after the dune. (d) All profiles with velocity streamlines. The unit of V_x is an averaged number of fluid particles per site flying along the direction of the flow.

stant. The density of fluid particles per site is taken equal to 1.5, the number of slow particles being twice the number of fast particles. Meanwhile, we use periodic boundary conditions in the horizontal direction so that fluid particles exiting from one side are instantaneously reinjected on the other. If the model of sediment transport uses non periodic boundary conditions, we have to reinject a uniform flow that does not depend on the topography. In this case, we filter the velocity vectors at the boundary across which the fluid particles are reinjected. This takes the form of permutations between particles in order to conserve the mean velocity. Moreover, in all cases, we impose a permanent forcing to simulate an unperturbed flow far above the bed. We achieve this by randomly replacing fluid particles moving along the opposite direction, by fluid particles moving along the prescribed direction of the flow. These replacements are homogeneously distributed within the entire system and concern 0.2% of the particles at each iteration.

C2. Rebound Dynamics

[81] The normal vector $\vec{n}$ is the vector perpendicular to the surface defined by sedimentary cells. Its three components are locally determined from the gradient using height differences between sedimentary cells located at 2 l_0 in all directions.

[82] Usually in LGCA, no-slip boundary conditions are imposed along the solid boundaries of the system. Then, when a particle is colliding with a solid boundary, it returns along the path from which it approached (a rotation of π of the velocity vector). Here, we implement two different sets of rebounds in order to introduce free-slip boundary conditions along the ceiling and a turbulent boundary layer on an irregular bottom.

[83] The top boundary conditions is therefore as follows: if the angle θ between the colliding particles and normal to the topography is between $-\pi/8$ and $\pi/8$, the particles return along the path from which they approached (a rotation of π of the velocity vector); if not, the colliding particle rebounds in a perpendicular direction according to the sign of θ (a rotation of $\pm\pi/2$ of the velocity vector). In comparison with a classical no-slip boundary condition, this rule introduces a free-slip boundary condition on a flat topography, as is the case along the ceiling.

[84] Along the bed, we keep the no-slip boundary conditions. In addition, because of the permanent motions of sedimentary cells on the flat bedrock, a smooth and flat bed form is never met during the computation. There is always a small-scale roughness and the direction of the normal to the surface varies from point to point. As a consequence, motions and collisions of fluid particles create a boundary layer across which the fluid velocity gradually increases (Figure C1).

Appendix D: Coupling Between the Model of Sediment Transport and the LGCA

[85] In order to take into account the simultaneous evolution of the topography and the bed shear, there is a permanent coupling between the model of sediment trans-

port and the LGCA. In this case, a major difficulty is to deal with the difference of time scales between the models. Some simplifications are required, and here we consider a time iteration scheme which is fully controlled by the model of sediment transport. In other words, there is no time delay associated with one motion cycle of fluid particles.

[86] From the initial conditions, the standard procedure is as follows. First, at $t = 0$ avalanches may occur to generate the stable initial bed elevation profile. Then, we stabilize the flow over this topography. This requires a number of iteration which is proportional to L, the characteristic length of the system. From this configuration of the flow and the spatial distribution of the bed shear stress the model of sediment transport can start, modifying one by one the population of active doublets at the end of the successive time increments (see Appendix B). With a return period T_r, avalanches may occur and one motion cycle of the lattice gas model is implemented. T_r is a parameter of the model, and here we chose $T_r = 0.1/\Lambda_0$, a value which is small compare to the characteristic time of erosion. Thus, the velocity field and the bed shear stress are regularly recalculated before they can be used to determine the future transitions of doublets.

[87] In this procedure, between two motion cycles of fluid particles the number of transitions in the model of sediment transport is not constant, fluctuating according to the topography and the topology of active doublets. More importantly, the entire configuration of the flow is recalculated over a time period which is much shorter than the time required to move one layer of sedimentary cells (i.e., $T_r \ll 1/\Lambda_e + 1/\Lambda_t + 1/\Lambda_c$). However, since the transitions of doublets are independent of fluid particles of the lattice gas model, a cell can undergo a transition from a fluid to a sedimentary state at sites where fluid particles are present. Where this happens, we consider that fluid particles are captured by the sedimentary cells, bouncing back and forth on the internal boundaries of these cells. When they undergo a transition from a sedimentary to a fluid state, fluid particles are released moving along the direction of their velocity vector at that specific time.

[88] **Acknowledgments.** The paper has been improved by constructive comments of A. Baas, the associate editor, and two anonymous reviewers. The authors are also grateful to E. Lajeunesse, F. Métivier, M. Tal, and B. Andreotti for their work on the different versions of the manuscript. Clément Narteau benefits from a Specific Targeted Research Project of the European Community (12975-E2C2). This work has been partially supported by the French Ministry of Research.

References

Anderson, R. S., and P. K. Haff (1988), Simulation of eolian saltation, *Science*, *241*, 820–823.

Andreotti, B. (2004), A two-species model of aeolian sand transport, *J. Fluid Mech.*, *510*, 47–70.

Andreotti, B., and P. Claudin (2007), Comment on "Minimal size of a barchan dune," *Phys. Rev. E*, *76*, 063301.1–063302.5, doi:10.1103/PhysRevE.76.063301.

Andreotti, B., P. Claudin, and S. Douady (2002), Selection of dune shapes and velocities: Part 2: A two-dimensional modelling, *Eur. Phys. J. B*, *28*, 341–352.

Baas, A., and J. Nield (2007), Modelling vegetated dune landscapes, *Geophys. Res. Lett.*, *34*, L06405, doi:10.1029/2006GL029152.

Bagnold, R. A. (1941), *The Physics of Blown Sand and Desert Dunes*, Methuen, London.

Bagnold, R. A. (1956), Flow of cohesionless grains in fluids, *Philos. Trans. R. Soc. London Ser. A*, *249*, 235–297.

Bak, P., C. Tang, and K. Wiesenfield (1988), Self-organised criticality, *Phys. Rev. A*, *38*, 364–374.

Breed, C., and T. Grow (1979), Morphology and distribution of dunes in sand seas observed by remote sensing, in *A Study of Global Sand Seas*, edited by E. McKee, *U.S. Geol. Surv. Prof. Pap., 1052*, pp. 252–302.

Bristow, C. S., S. D. Bailey, and N. Lancaster (2000), The sedimentary structure of linear sand dunes, *Nature*, *406*, 56–59.

Bristow, C. S., G. Duller, and N. Lancaster (2007), Age and dynamics of linear dunes in the Namib desert, *Geology*, *35*, 555–558.

Charru, F. (2006), Selection of the ripple length on a granular bed, *Phys. Fluids*, *18*, 121–508.

Chopard, B., and M. Droz (1998), *Cellular Automata Modeling of Physical Systems*, Cambridge Univ. Press, Cambridge, U. K.

Claudin, P., and B. Andreotti (2006), A scaling law for aeolian dunes on Mars, Venus, Earth, and for subaqueous ripples, *Earth Plan. Sci. Lett.*, *252*, 30–44.

d'Humières, D., P. Lallemand, and U. Frisch (1986), Lattice gas models for 3-D hydrodynamics, *Europhys. Lett.*, *2*, 291–297.

Durán, O., and H. Herrmann (2006), Vegetation against dune mobility, *Phys. Rev. Lett.*, *97*, 188001.1–181001.4.

Durán, O., V. Schwämmle, and H. Herrmann (2005), Breeding and solitary wave behavior of dunes, *Phys. Rev. E*, *72*, 021308.1–021308.5.

Elbelrhiti, H., P. Claudin, and B. Andreotti (2005), Field evidence for surface-wave-induced instability of sand dunes, *Nature*, *437*, 720–723.

Elbelrhiti, H., B. Andreotti, and P. Claudin (2008), Barchan dune corridors: Field characterization and investigation of control parameters, *J. Geophys. Res.*, *113*, F02S15, doi:10.1029/2007JF000767.

Engelund, F. (1970), Instability of erodible beds, *J. Fluid Mech.*, *42*, 225–244.

Engelund, F., and J. Fredsøe (1982), Sediment ripples and dunes, *Ann. Rev. Fluid Mech.*, *14*, 13–37.

Ewing, R., G. Kocurek, and L. Lake (2006), Pattern analysis of dune-field parameters, *Earth Surf. Processes Landforms*, *31*, 1176–1191, doi:10.1002/esp.1312.

Fredsøe, J. (1974), On the development of dunes in erodible channels, *J. Fluid Mech.*, *64*, 1–16.

Frisch, U., B. Hasslacher, and Y. Pomeau (1986), Lattice-gas automata for the Navier-Stokes equation, *Phys. Rev. Lett.*, *56*, 1505–1508.

Hardy, J., O. de Pazzis, and Y. Pomeau (1976), Molecular dynamics of a classical lattice gas: Transport properties and time correlation functions, *Phys. Rev. A*, *13*, 1949–1961.

Hersen, P. (2004), On the crescentic shape of barchan dunes, *Eur. Phys. J. B*, *37*, 507–514.

Hersen, P., K. H. Andersen, H. Elbelrhiti, B. Andreotti, P. Claudin, and S. Douady (2004), Corridors of barchan dunes: Stability and size selection, *Phys. Rev. E*, *69*, 011304.1–011304.12.

Hunt, J. C. R., S. Leibovich, and K. J. Richards (1988), Turbulent wind flow over smooth hills, *Q. J. R. Meteorol. Soc.*, *114*, 1435–1470.

Jackson, P. S., and J. C. R. Hunt (1975), Turbulent wind flow over a low hill, *Q. J. R. Meteorol. Soc.*, *101*, 929–955.

Kennedy, J. (1963), The mechanics of dunes and antidunes in erodible bed channels, *J. Fluid Mech.*, *16*, 521–544.

Kocurek, G., and R. Ewing (2005), Aeolian dune field self-organization: Implications for the formation of simple versus complex dune-field patterns, *Geomorphology*, *72*, 10–94.

Kocurek, G., K. Havholm, M. Deynoux, and R. Blakey (1991), Amalgamated accumulations resulting from climatic and eustatic changes, Akchar Erg, Mauritania, *Sedimentology*, *38*, 751–772.

Kroy, K., G. Sauermann, and H. J. Herrmann (2002a), Minimal model for sand dunes, *Phys. Rev. Lett.*, *88*, 054301.1–054301.4.

Kroy, K., G. Sauermann, and H. J. Herrmann (2002b), Minimal model for aeolian sand dunes, *Phys. Rev. E*, *66*, 031302.1–031302.18.

Lancaster, N. (1995), *Geomorphology of Desert Dunes*, Routledge, New York.

McKee, E. (1979), Introduction to a study of global sand seas, in *A Study of Global Sand Seas*, edited by E. McKee, *U.S. Geol. Surv. Prof. Pap., 1052*, pp. 3–19.

Meyer-Peter, E., and R. Müller (1948), Formulas for bed load transport, in *Proceedings of the 2nd Meeting of the International Association for Hydraulic Structures Research*, pp. 39–64, Inter. Assoc. for Hydraul. Res., Delft, Netherlands.

Momiji, H., and A. Warren (2000), Relations of sand trapping efficiency and migration speed of transverse dunes to wind velocity, *Earth Surf. Processes Landforms*, *25*, 1069–1084.

Narteau, C., J.-L. Le Mouël, J. Poirier, E. Sepúlveda, and M. G. Shnirman (2001), On a small scale roughness of the core-mantle boundary, *Phys. Earth Planet. Int.*, *191*, 49–61.

Nishimori, H., and N. Ouchi (1993), Computational models for sand ripple and sand dune formation, *Int. J. Mod. Phys. B*, *7*, 2025–2034.

Nishimori, H., M. Yamasaki, and K. H. Andersen (1999), A simple model for the various pattern dynamics of dunes, *Int. J. Mod. Phys. B*, *12*, 257–272.

Parker, G. (1975), Sediment inertia as cause of river antidunes, *J. Hydraul. Div.*, *101*, 211–221.

Parteli, E., and H. Herrmann (2007), Dune formation on the present Mars, *Phys. Rev. E*, *76*, 041307.1–041307.16.

Parteli, E., O. Durán, and H. Herrmann (2007a), Reply to ''Comment on ''minimal size of a barchan dune'','' *Phys. Rev. E*, *76*, 063302.1–063302.5, doi:10.1103/PhysRevE.76.063302.

Parteli, E. J. R, O. Durán, and H. J. Herrmann (2007b), Minimal size of a barchan dune, *Phys. Rev. E*, *75*, 011301.1–011301.10.

Rasmussen, K. R., J. D. Iversen, and P. Rautaheimo (1996), Saltation and wind flow interaction in a variable slope wind tunnel, *Geomorphology*, *17*, 19–28.

Reynolds, A. (1965), Waves on the erodible bed of an open channel, *J. Fluid Mech.*, *22*, 113–133.

Richards, K. (1980), The formation of ripples and dunes on an erodible bed, *J. Fluid Mech.*, *99*, 567–618.

Rothman, D. H., and S. Zaleski (2004), *Lattice-Gas Cellular Automata: Simple Models of Complex Hydrodynamics*, Cambridge Univ. Press, Cambridge, U. K.

Sauermann, G., K. Kroy, and H. J. Herrmann (2001), Continuum saltation model for sand dunes, *Phys. Rev. E*, *6403*, 031305.1–031305.10.

Sykes, R. I. (1980), An asymptotic theory of incompressible turbulent boundary layer flow over a small hump, *J. Fluid Mech.*, *101*, 647–670.

Taylor, P., P. Mason, and E. Bradley (1987), Boundary-layer flow over low hills, *Boundary Layer Meteorol.*, *39*, 107–132.

Ungar, J. E., and P. K. Haff (1987), Steady state saltation in air, *Sedimentology*, *34*, 289–299.

Werner, B. T. (1995), Eolian dunes: Computer simulations and attractor interpretation, *Geology*, *23*, 1107–1110.

Werner, B. T., and G. Kocurek (1997), Bed-from dynamics: Does the tail wag the dog?, *Geology*, *25*, 771–774.

Wiggs, G. F. S. (2001), Desert dune processes and dynamics, *Prog. in Phys. Geogr.*, *25*, 53–79.

Wolfram, S. (1986), *Theory and Application of Cellular Automata*, World Sci., Singapore.

P. Claudin, Laboratoire de Physique et de Mécanique des Milieux Hétérogènes, UMR 7636, École Supérieure de Physique et de Chimie Industrielles de la Ville de Paris, University Paris 6 and Paris 7, CNRS, 10 Rue Vauquelin, F-75231 Paris CEDEX 05, France. (claudin@pmmh.espci.fr)

C. Narteau and D. Zhang, Laboratoire de Dynamique des Fluides Géologiques, UMR 7154, Institut de Physique du Globe de Paris, University Paris 7, CNRS, 4 Place Jussieu, F-75252 Paris CEDEX 05, France. (narteau@ipgp.jussieu.fr; dzhang@ipgp.jussieu.fr)

O. Rozier, Service Informatique, UMR 7154, Institut de Physique du Globe de Paris, University Paris 7, CNRS, 4 Place Jussieu, F-75252 Paris CEDEX 05, France. (rozier@ipgp.jussieu.fr)